

Deep Learning based Absorption Tomography for Combustion Diagnostics

Arnab Mahanti*, Satheesh K.[†], Deepak Mishra[‡], Rajesh Sadanandan[§]
Indian Institute of Space Science and Technology, Thiruvananthapuram, Kerala, 695547

Laser absorption spectroscopy combined with nonlinear tomography has proved to be an effective technique for measurement of critical flow variables of a combustion system. However, the computationally intensive nature of the reconstruction process imposes limitations to the applicability of this technique. Non-conventional techniques based on neural networks have emerged recently to tackle this problem. Here, a neural network has been implemented to simultaneously reconstruct 2D temperature and concentration fields from synthetically generated integrated absorbance data. The trained network is capable of reconstruction within a time of 30-40 ms on a CPU only system with two virtualized cores of Intel Xeon @ 2.2GHz. Very low average errors of 0.66% and 0.87% for unimodal distributions and 1.03% and 1.2% for multimodal distributions are achieved for the reconstruction of temperature and concentration fields respectively.

Keywords: Combustion Diagnostics, TDLAS, NTAS, Y-Net

I. Introduction

The fundamental parameters required for characterizing and diagnosing efficiency of any combustion system are temperature, pressure, and species concentrations. Laser Absorption Spectroscopy (LAS) is quickly becoming a promising non-intrusive method for extracting this information from combustion environments [1, 2]. However, being a line-of-sight (LOS) technique absorption spectroscopy does not possess spatial resolution to resolve the highly non-uniform and unsteady flow fields and species distributions [3]. This limitation can be alleviated by using tomography alongside LAS, by a technique called Tomographic Absorption Spectroscopy (TAS), for both spatially resolved and temporally resolved measurements [4]. Nonlinear TAS (NTAS), based on the concept of nonlinear tomography is capable of simultaneously recovering temperature, pressure, and species concentration fields, but requires solving a large system of highly nonlinear integral equations [5–8]. The inversion is usually achieved by solving a global optimization problem which has a very high computational cost [9]. In recent years, Convolution Neural Networks (CNN) have evolved to be capable of building efficient maps between two datasets and is becoming the framework of choice in image classification, detection, and segmentation. Owing to their static nature at runtime, they have a potential of showing improved performance over traditional regression algorithms. A successful scientific theory of Absorption Spectroscopy paves the way of synthetically generating accurate NTAS data to train them. They have been applied to directly reconstruct fields from projection data and have showed significant improvements over traditional techniques such as simulated annealing [9]. A specific class of CNN called Y-Net have been established as a one-to-two deep learning framework for simultaneous reconstruction of phase and intensity data for the holographic reconstruction problem [10]. Considering the similarity of the nature of the problem, Y-Nets seem to be a viable option for simultaneous reconstruction of multiple fields from NTAS data. Here, we present a simulative study on computed NTAS data to explore the possibility of applying Y-Nets to simultaneously reconstruct 2D temperature and species concentration fields of a laminar non-premixed flame configuration stabilized in a Bunsen burner as shown schematically in Fig. 1. The NTAS data have been synthetically generated for assumed temperature and species concentration distributions which are of radially symmetric nature, typical of this kind of combustion environment.

*B.Tech student, Department of Aerospace Engineering, arnab.sc19b005@ug.iist.ac.in

[†] Associate Professor, Department of Aerospace Engineering, satheeshk@iist.ac.in

[‡] Professor, Department of Avionics, deepak.mishra@iist.ac.in

[§] Associate Professor, Department of Aerospace Engineering, rajeshsadanandan@iist.ac.in

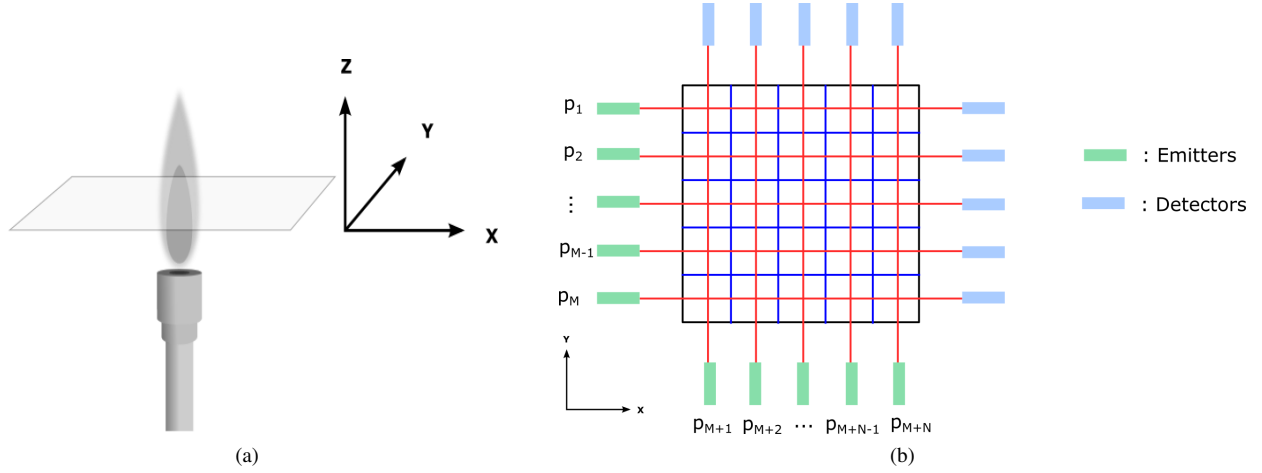


Fig. 1 Schematic of the NTAS configuration and the plane of measurement is shown in (a). The region of interest has been discretized into a $M \times N$ square grid as shown in (b). The projected beams are shown as red lines.

II. Mathematical Formulation

The NTAS problem can be formulated mathematically for gaseous mediums using the Beer-Lambert law, which states that if a radiation of frequency ν with initial intensity I_0 is attenuated to intensity I after passing through the medium, then:

$$p(\nu) = \int_a^b \sum_i S(T(l), \nu_i) \cdot \Phi(T(l), X(l), (\nu_i - \nu)) \cdot P \cdot X(l) \, dl \quad (1)$$

where $p(\nu)$ is the absorbance at frequency ν ; l is the path parameter; a and b are the bounds of the region of interest (ROI) along l ; $T(l)$ and $X(l)$ are the temperature of the medium and species concentration distributions of the absorbing species along l ; P is the pressure; Φ is the normalized line-shape function; and $S(T(l), \nu_i)$ is the line strength of the i^{th} non-negligible transition centered at ν_i which contributes to the absorbance at frequency ν [6].

Appropriate choice of the function Φ needs to be done, dictated by the dominant line-broadening mechanisms. An often-chosen candidate is the Voigt shape function, which is defined as a convolution in ν between the Gaussian line-shape function and the Lorentzian line-shape function [11, 12]. A schematic is shown in Fig. 1, where the ROI is discretized into a square grid of size $M \times N$, and a total of $M + N$ laser projections are taken from left to right and bottom to top.

Discretizing the ROI into a $M \times N$ square grid and replacing the integrals in (1) with sums yields the following system of nonlinear equations:

$$p(l_k, \nu) = \sum_q \sum_i S(T_q, \nu_i) \cdot \Phi(T_q, X_q, (\nu_i - \nu)) P X_q \Delta_{k,q} \quad (2)$$

where k is the index of projection; q is the index of the grid cell; T_q and X_q are the temperature and concentration in the q^{th} grid cell respectively; and $\Delta_{k,q}$ is the path length travelled by the laser along k^{th} projection in the q^{th} grid cell.

In general, combustion environments have limited access and hence the system (2) is often rank-deficient [7]. Besides, the functions Φ and S are nonlinear, due to which (2) cannot be inverted directly. This then requires setting up an optimization problem to solve the system. Traditional algorithms such as simulated annealing can take up to ten hours to reconstruct a single case of temperature distribution on a 40×40 grid [9]. In contrast all the operations in a trained neural network are fixed and thus take a constant time during prediction, hence they are static and have the potential of being four to five orders of magnitude faster than any of the traditional techniques. The accuracy of the reconstruction can be assured by the Universal Approximation Theorem, which states that a multi-layered perceptron can approximate any continuous function to arbitrary precision given a nonlinear activation function and enough number of hidden layers [13]. Furthermore, it has been shown that CNNs are universal approximators which means they can achieve the same functionality as that of a multilayered perceptron model [14]. This opens the possibility of applying CNNs such as

Center frequency $\nu(\text{cm}^{-1})$	Line Strength S(298K) $(\text{cm}^{-1}/(\text{molecule} \times \text{cm}^{-2}))$	Lower energy state E (cm^{-1})
7179.7524	1.70×10^{-22}	1216.194
7180.39972	5.56×10^{-22}	224.8384
7181.15578	1.50×10^{-20}	136.7617
7182.20911	1.58×10^{-21}	42.3717
7182.94962	3.77×10^{-21}	142.2785
7183.01579	4.07×10^{-22}	134.9016
7185.59657	1.98×10^{-22}	1045.0583
7185.5973	5.93×10^{-22}	1045.0578

Table 1 Spectral lines of H_2O molecules used for NTAS

Y-Nets to solve the NTAS problem. The aim is to establish an approximation of the map from multispectral integrated absorbance data to the temperature and concentration fields for a subspace of all possible phantoms which contain three independent Gaussian modes.

III. Dataset generation

Two training datasets for the neural network have been generated on a 50×50 grid with 100 beams and 8 absorption lines for H_2O molecules in an air bath using the process depicted in [15]. The dataset consists of pairs of temperature and concentration phantoms. One dataset consists of unimodal 2D Gaussian phantoms, whereas the other consists of multimodal phantoms composed of three individual 2D Gaussian phantoms. They can be represented using the following expression:

$$P = \sum_{i=1}^m a_i \cdot \exp \left[-\frac{(x - x_{0,i})^2 + (y - y_{0,i})^2}{2c_i^2} \right] \quad (3)$$

where a_i are the amplitudes of the modes, c_i are the variances and $(x_{0,i}, y_{0,i})$ are the peak locations. The non-dimensionalized domain consists of the region $[0, 1] \times [0, 1]$. For the unimodal dataset $m = 1$ and a is sampled uniformly from the range $[0.3, 1]$; (x_0, y_0) is sampled uniformly from $[0.1, 0.9] \times [0.1, 0.9]$; and c is sampled uniformly from $[0.1, 1]$. For the multimodal dataset $m = 3$ and the first mode is generated similar to the unimodal case but with c uniformly sampled from $[0.15, 0.45]$. For the other two modes a_i is sampled uniformly from $[0, 1]$. Relative positions of the peaks with respect to the first mode are sampled as (r, θ) pair from $[c_1, 1] \times [0, 2\pi]$ and are added to the position of the first mode. In case they are out of the region $[0.1, 0.9] \times [0.1, 0.9]$ they are wrapped around to fit inside the region. Multiple modes together forms phantoms with one, two or three peaks in this case. The multimodal phantoms with one peaks are included to have distorted Gaussian distributions. This is to ensure that the network trained on the multimodal dataset also works for cases when the distribution is unimodal. Each temperature phantom is normalized in the range $[1000 \text{ K}, 2000 \text{ K}]$ and each concentration (mole fraction) phantom is normalized in the range $[0.01, 0.25]$. In the current study the temperature and species concentration phantoms are uncorrelated. The Centerline frequency, linestrength and lower energy state of the 8 transitions used to calculate the NTAS projections are selected from the HITEMP database and are listed in Table 1. For the unimodal dataset a total of 10000 samples were generated among which 9000 are used to train the neural network, whereas 1000 samples are used for validation. For the multimodal dataset a total of 20000 generated samples are split into train and validation datasets of sizes 18000 and 2000, respectively.

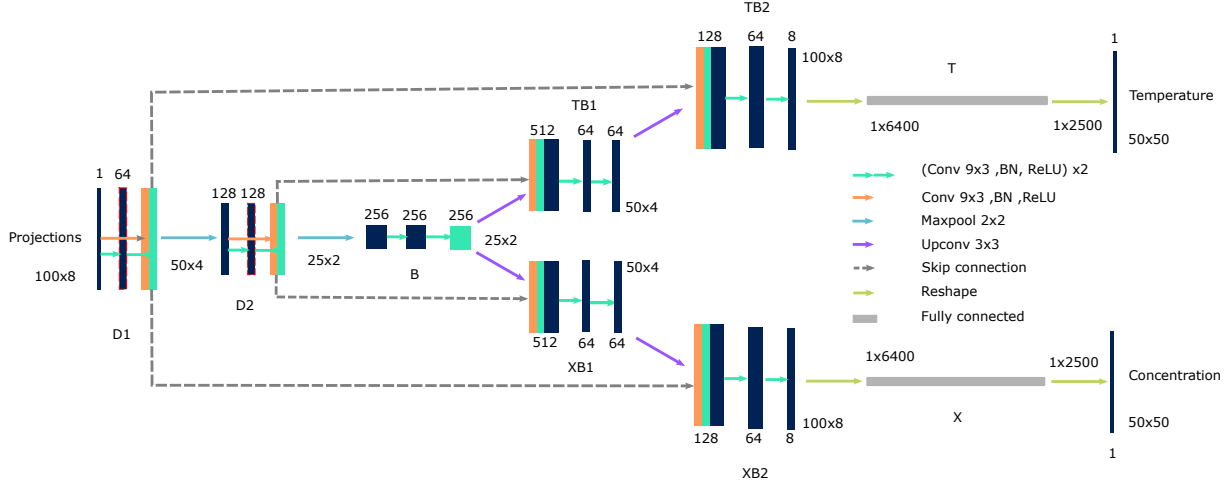


Fig. 2 A schematic of the Y-Net used for simultaneous reconstruction of the temperature and concentration fields. Each of the blocks represent a feature map which is extracted after an operation as depicted by the arrows in between. The numbers on the left of the block represent the size of the feature map. The numbers on the top and bottom of the blocks represent the depth of the feature map. Red dotted boxes are intermediate outputs shown for visualization purposes only.

IV. Network architecture and training

The synthetically generated NTAS projections are supplied to the network shown in Fig. 2 in minibatches of size 50 and 100 for the unimodal and multimodal cases, respectively [16]. The two predictions of the network, each of size 50×50 are stacked together to form a single output of size $2 \times 50 \times 50$ during training and is compared with the ground truth. The mean square error (MSE) between the predictions and the ground truth is chosen as the loss function to be optimized. The MSE is defined as:

$$\frac{1}{B} \cdot \frac{1}{M \times N} \cdot \sum_{i=1}^B \sum_{j=1}^{M \times N} \left(y_j^{(i)} - o_j^{(i)} \right)^2 \quad (4)$$

where B is the minibatch size; $M \times N$ (here 50×50) is the grid size; $y_j^{(i)}$ and $o_j^{(i)}$ are the ground truth values and predictions respectively of the j^{th} grid cell in the i^{th} case of the minibatch. The optimizer algorithm chosen for training is Adaptive moment estimation (ADAM) with a weight decay of 0.0003 [17]. To validate the network with a validation set of size V, the maximum relative error between the prediction and ground truth has been used, which is defined as follows:

$$e = \frac{1}{V} \sum_{i=1}^V \max_{j=1}^{M \times N} \left(\left| y_j^{(i)} - o_j^{(i)} \right| \right) \quad (5)$$

All the convolution kernels are initialized via Kaiming initialization before the training process [18]. The nonlinear activation function used is ReLU (Rectified Linear Unit), which is defined as follows:

$$ReLU(x) = \begin{cases} x & x > 0 \\ 0 & x \leq 0 \end{cases} \quad (6)$$

The network consists of 40,321,576 learnable parameters. The learning rate has been varied starting from 0.5×10^{-4} to 1.0×10^{-8} during the training process. The model is coded in Python with the machine learning framework PyTorch. The model has been trained on a system equipped with an NVIDIA Tesla T4 GPU with 16GB VRAM. The average VRAM requirement during training is 8GB. The time required to train the network is approximately 4 hrs. A convergence plot of the network has been shown in Fig. 3.

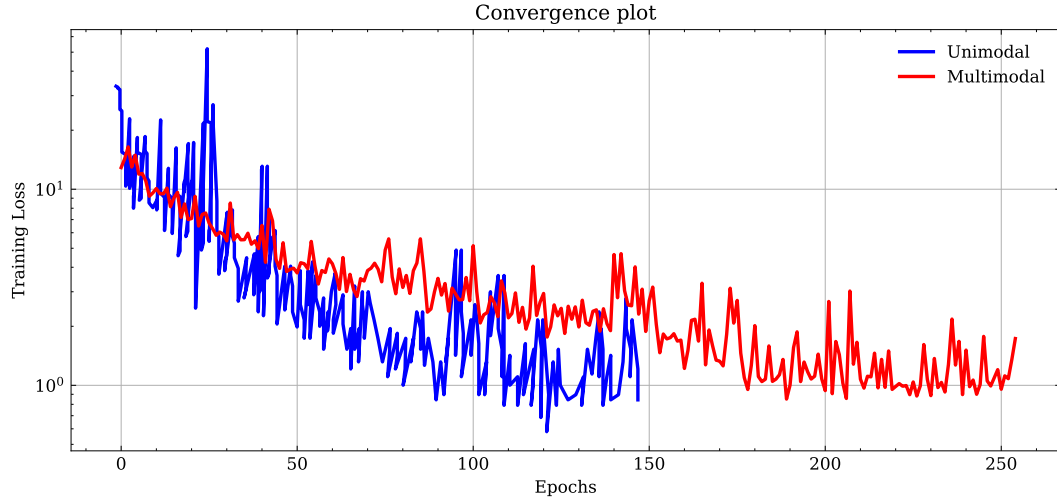


Fig. 3 Convergence plot of the designed network. The unimodal case converges around 150 epochs whereas the multimodal case converges around 250 epochs.

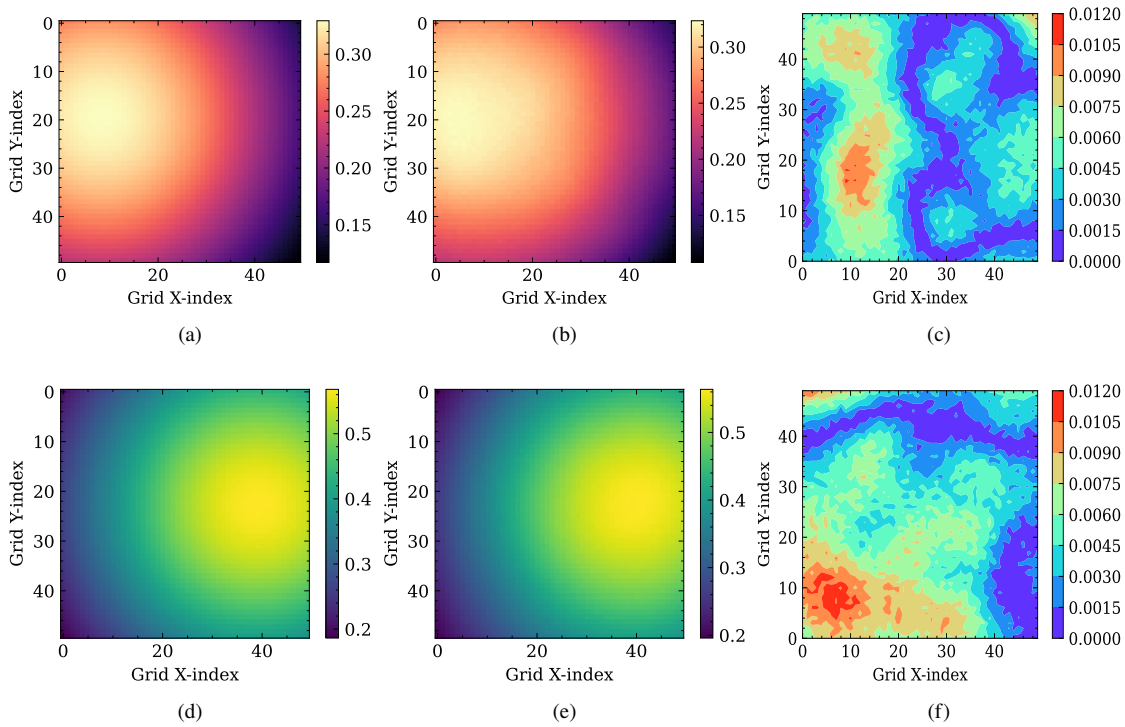


Fig. 4 Comparison of reconstructed normalized distributions with ground truth distributions for a sample case. The subfigures (a) and (b) are the ground truth and reconstructed temperature distributions, respectively, whereas (d) and (e) are the ground truth and reconstructed concentration distributions, respectively. The subfigures (c) and (f) represent the contour plots of point to point relative errors in predicted temperature and concentration fields, respectively.

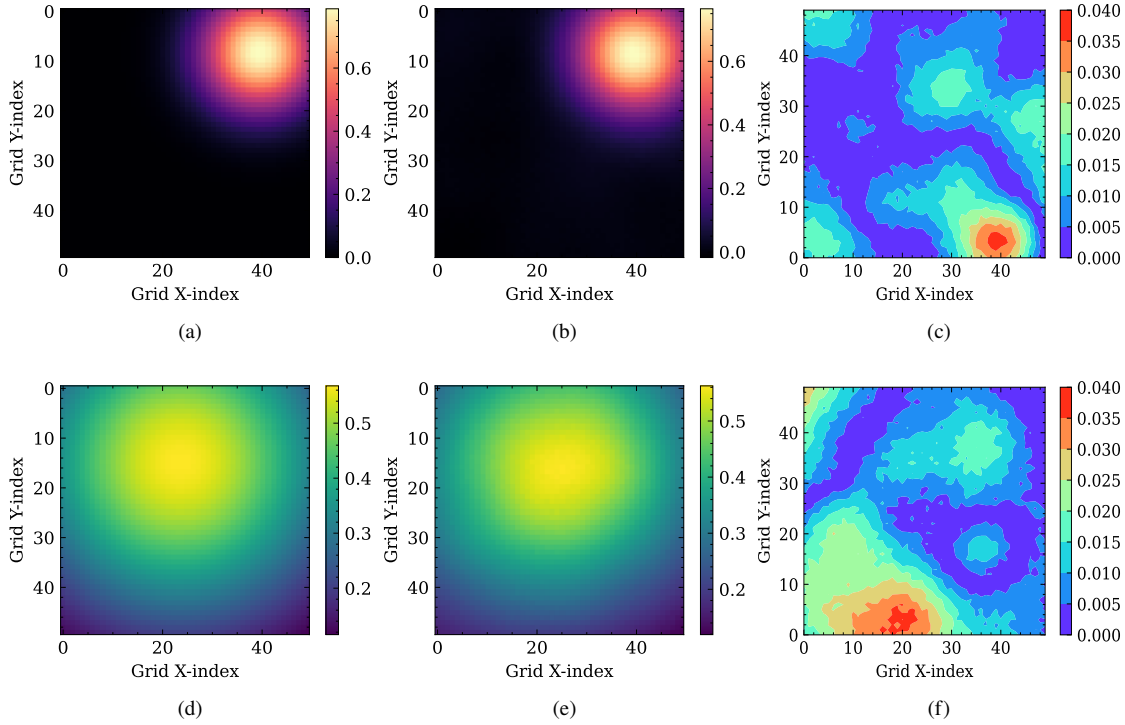


Fig. 5 Comparison of reconstructed normalized distributions with ground truth for a sample case with sharp distributions. The subfigures (a) and (b) are the ground truth and reconstructed temperature distributions, respectively, whereas (d) and (e) are the ground truth and reconstructed concentration distributions, respectively. The subfigures (c) and (f) represent the contour plots of point to point relative errors in predicted temperature and concentration fields, respectively.

V. Results

A. Reconstruction

The trained networks have been used to reconstruct the temperature and concentration distributions. Two random samples of reconstructions of unimodal case are shown in Fig. 4 and Fig. 5. Figure 6 and Fig. 7 shows the reconstructions for multimodal case. The outputs are shown as normalized distributions. The reconstruction has been done on a CPU only system with two virtualized cores of Intel Xeon @ 2.2 GHz. The average time required for a single reconstruction is 30ms and 40ms for unimodal and multimodal cases, respectively. This is a significant improvement over the previously discussed simulated annealing algorithm which requires 10h to reconstruct a single case of temperature distribution on a 40×40 grid[9]. The results can be further improved by tuning and implementing the model to run directly on hardware rather than an interpreter as in Python.

For the quantification of reconstruction error, average point to point relative error of the reconstructed distribution is taken. The relative reconstruction error for unimodal and multimodal cases with 50 test samples each are shown in Fig. 8.

1. Unimodal Case

The average relative error in reconstructed temperature distribution is 0.66% and that in reconstructed concentration distribution is 0.87%. The maximum and minimum relative error in reconstructed temperature distribution is 1.42% and 0.18% respectively. Whereas the maximum and minimum relative error in reconstructed concentration distribution is 1.86% and 0.31% respectively. It is observed that the smoothness precondition is preserved by the neural network even for sharp distributions and the reconstructed results are without any major spikes as encountered in many reconstruction scenarios through traditional methods.

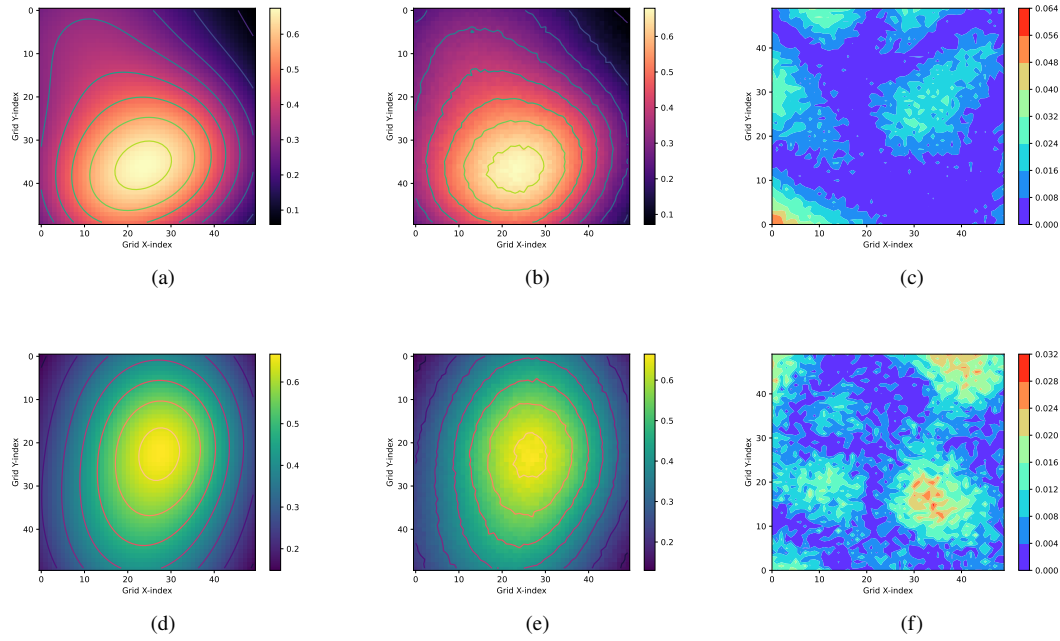


Fig. 6 Comparison of reconstructed normalized distributions with ground truth for a sample case with distorted gaussian distributions. The subfigures (a) and (b) are the ground truth and reconstructed temperature distributions, respectively, whereas (d) and (e) are the ground truth and reconstructed concentration distributions, respectively. The subfigures (c) and (f) represent the contour plots of point to point relative errors in predicted temperature and concentration fields, respectively.

2. Multimodal Case

The relative reconstruction error in the multimodal case is higher than the unimodal case. The average relative error in reconstructed temperature distribution is 1.03% and that in reconstructed concentration distribution is 1.2%. The maximum and minimum relative error in reconstructed temperature distribution is 2.26% and 0.63% respectively. Whereas the maximum and minimum relative error in reconstructed concentration distribution is 2.98% and 0.64% respectively. It is observed that the smoothness precondition although preserved, is not on par with the unimodal case.

B. Noise Immunity

In practical applications, the NTAS data will contain experimental noise. Hence, the immunity of the network to reconstruct correct distributions which satisfy the smoothness preconditions from input data corrupted by noise must be studied. For this Gaussian noise of varying intensities are added to the input data and the relative reconstruction errors are plotted for both unimodal and multimodal cases in Fig. 9.

It is seen that the trained network for unimodal case is much more immune to noise than the network for multimodal case. This is expected as the unimodal network has added precondition about the nature of the distributions whereas in the multimodal case as the distribution does not have such precondition, distinguishing noise from actual data is difficult. It is also seen that for both the networks reconstruction of the temperature field is more immune to noise than that of the concentration field.

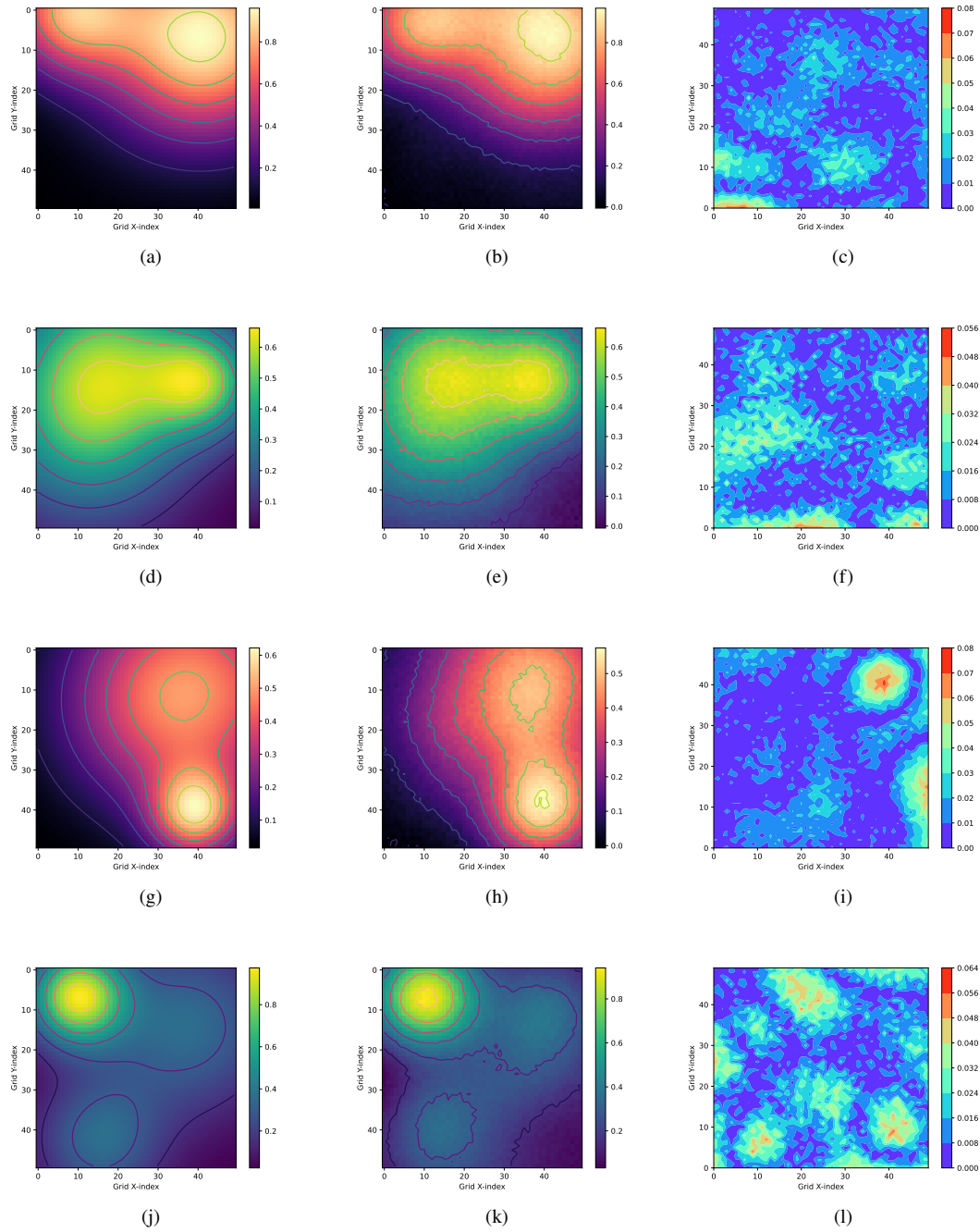


Fig. 7 Comparison of reconstructed normalized distributions with ground truth for sample cases with multimodal distributions. The subfigures (a),(g) and (b),(h) are the ground truths and reconstructed temperature distributions, respectively, whereas (d),(j) and (e),(k) are the ground truth and reconstructed concentration distributions, respectively. The subfigures (c),(i) and (f),(l) represent the contour plots of point to point relative errors in predicted temperature and concentration fields, respectively.

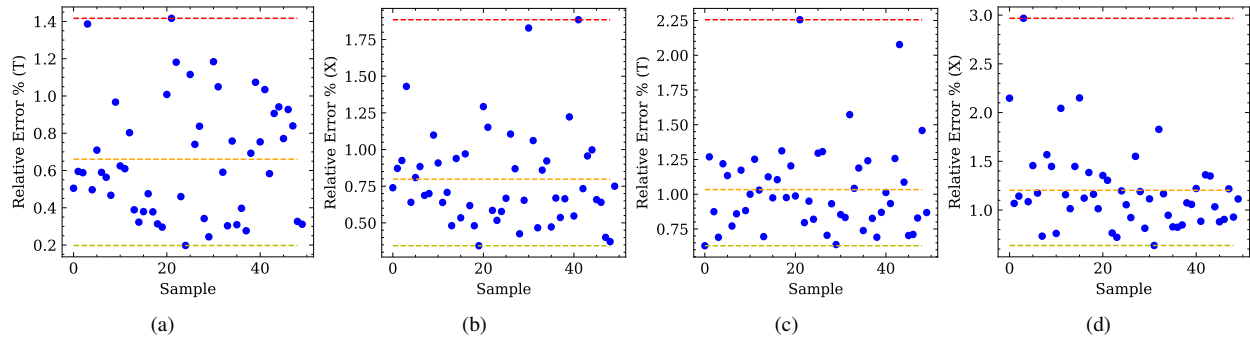


Fig. 8 Relative error in reconstructed fields for 50 random test samples are shown in (a),(b) and (c),(d) for unimodal and multimodal cases, respectively. The yellow line shows the average reconstruction error. The red and green lines show the maximum and minimum reconstruction error, respectively.

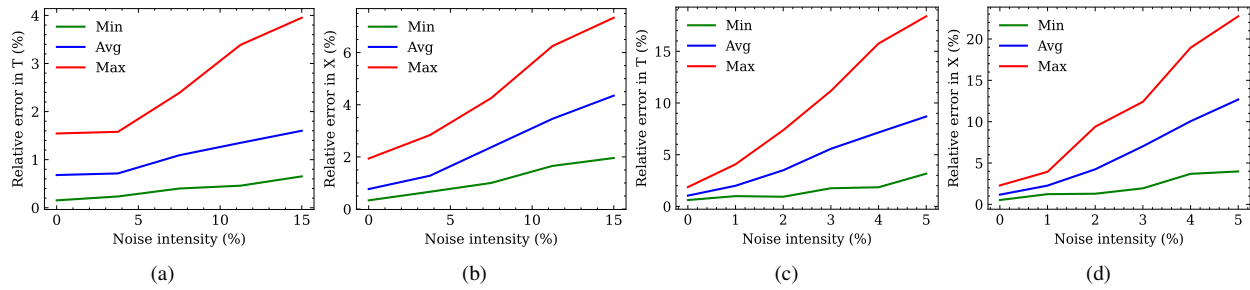


Fig. 9 Variation of relative reconstruction error with input noise intensity is shown in (a),(b) and (c),(d) for unimodal and multimodal cases, respectively. The green, blue and red lines represent minimum, average and maximum relative reconstruction errors, respectively.

VI. Conclusion

In summary, it has been demonstrated that, Y-Nets are suitable for efficient simultaneous reconstruction of temperature and species concentration fields and can be applied to the NTAS problem with acceptable accuracy and fast reconstruction time for multimodal distributions. In the current study, average errors of 0.66% and 0.87% for unimodal distributions and 1.03% and 1.2% for multimodal distributions were achieved for the reconstruction of temperature and concentration fields, respectively. However, there is no correlation between the temperature and species concentration phantoms used during generation of the datasets. Since the system is rank deficient, incorporation of their interdependence may lead to better noise immunity and more accurate reconstructions.

Acknowledgments

Generation of the datasets and training of the neural network have been done in the High-Performance Computing Facility of Indian Institute of Space Science and Technology, Thiruvananthapuram.

References

- [1] Qu, Q., Cao, Z., Xu, L., Liu, C., Chang, L., and McCann, H., "Reconstruction of two-dimensional velocity distribution in scramjet by laser absorption spectroscopy tomography," *Appl. Opt.*, Vol. 58, No. 1, 2019, pp. 205–212. <https://doi.org/10.1364/AO.58.000205>.
- [2] Goldenstein, C. S., Spearrin, R., Jeffries, J. B., and Hanson, R. K., "Infrared laser-absorption sensing for combustion gases," *Progress in Energy and Combustion Science*, Vol. 60, 2017, pp. 132–176. <https://doi.org/10.1016/j.pecs.2016.12.002>.

- [3] Cai, W., and Kaminski, C. F., "Tomographic absorption spectroscopy for the study of gas dynamics and reactive flows," *Progress in Energy and Combustion Science*, Vol. 59, 2017, pp. 1–31. <https://doi.org/https://doi.org/10.1016/j.pecs.2016.11.002>.
- [4] Liu, C., Cao, Z., Lin, Y., Xu, L., and McCann, H., "Online Cross-Sectional Monitoring of a Swirling Flame Using TDLAS Tomography," *IEEE Transactions on Instrumentation and Measurement*, Vol. 67, No. 6, 2018, pp. 1338–1348. <https://doi.org/10.1109/TIM.2018.2799098>.
- [5] Cai, W. and Kaminski, C. F., "Multiplexed absorption tomography with calibration-free wavelength modulation spectroscopy," *Applied Physics Letters*, Vol. 104, No. 15, 2014, p. 154106. <https://doi.org/10.1063/1.4871976>.
- [6] Cai, W. and Kaminski, C. F., "A tomographic technique for the simultaneous imaging of temperature, chemical species, and pressure in reactive flows using absorption spectroscopy with frequency-agile lasers," *Applied Physics Letters*, Vol. 104, No. 3, 2014, p. 034101. <https://doi.org/https://doi.org/10.1063/1.4862754>.
- [7] Dai, J., Yu, T., Xu, L., and Cai, W., "On the regularization for nonlinear tomographic absorption spectroscopy," *Journal of Quantitative Spectroscopy and Radiative Transfer*, Vol. 206, 2018, pp. 233–241. <https://doi.org/https://doi.org/10.1016/j.jqsrt.2017.11.016>.
- [8] Ma, L., and Cai, W., "Determination of the optimal regularization parameters in hyperspectral tomography," *Appl. Opt.*, Vol. 47, No. 23, 2008, pp. 4186–4192. <https://doi.org/10.1364/AO.47.004186>.
- [9] Huang, J., Liu, H., Dai, J., and Cai, W., "Reconstruction for limited-data nonlinear tomographic absorption spectroscopy via deep learning," *Journal of Quantitative Spectroscopy and Radiative Transfer*, Vol. 218, 2018, pp. 187–193. <https://doi.org/https://doi.org/10.1016/j.jqsrt.2018.07.011>.
- [10] Wang, K., Dou, J., Kemao, Q., Di, J., and Zhao, J., "Y-Net: a one-to-two deep learning framework for digital holographic reconstruction," *Opt. Lett.*, Vol. 44, No. 19, 2019, pp. 4765–4768. <https://doi.org/10.1364/OL.44.004765>.
- [11] Strow, L. L., "Line Mixing In Infrared Atmospheric Spectra," *SPIE Proceedings*, Vol. 928, SPIE, 1988, pp. 194–212. <https://doi.org/10.1117/12.975628>.
- [12] Iino, M., "Transition from lorentzian to gaussian line shape of magnetization transfer spectrum in bovine serum albumin solutions," *Magnetic Resonance in Medicine*, Vol. 32, No. 4, 1994, pp. 459–463. <https://doi.org/https://doi.org/10.1002/mrm.1910320406>.
- [13] Hornik, K., Stinchcombe, M., and White, H., "Multilayer feedforward networks are universal approximators," *Neural Networks*, Vol. 2, No. 5, 1989, pp. 359–366. [https://doi.org/https://doi.org/10.1016/0893-6080\(89\)90020-8](https://doi.org/https://doi.org/10.1016/0893-6080(89)90020-8).
- [14] Zhou, D., "Universality of Deep Convolutional Neural Networks," 2018. <https://doi.org/10.48550/ARXIV.1805.10769>.
- [15] Golui, D. K., "Tunable Diode Laser Absorption Based Sensors for Combustion Diagnostics: Molecular Spectroscopic Modeling Thermometry," B.Tech Report, Indian Institute of Space Science and Technology, Thiruvananthapuram, Kerala, India, 2020.
- [16] Li, M., Zhang, T., Chen, Y., and Smola, A. J., "Efficient Mini-Batch Training for Stochastic Optimization," *Proceedings of the 20th ACM SIGKDD International Conference on Knowledge Discovery and Data Mining*, Association for Computing Machinery, New York, NY, USA, 2014, p. 661–670. <https://doi.org/10.1145/2623330.2623612>.
- [17] Kingma, D. P., and Ba, J., "Adam: A Method for Stochastic Optimization," *3rd International Conference on Learning Representations*, 2015. <https://doi.org/http://arxiv.org/abs/1412.6980>.
- [18] He, K., Zhang, X., Ren, S., and Sun, J., "Deep Residual Learning for Image Recognition," *2016 IEEE Conference on Computer Vision and Pattern Recognition (CVPR)*, 2016, pp. 770–778. <https://doi.org/https://doi.org/10.48550/arXiv.1512.03385>.